

## SUPPORTING INFORMATION

# Orbital angular momentum and energy loss characterization of plasmonic excitations in metallic nanostructures in TEM

*Matteo Zanfrognini<sup>1,2</sup>, Enzo Rotunno<sup>2</sup>, Stefano Frabboni<sup>1,2</sup>, Alicia Sit<sup>3</sup>, Ebrahim Karimi<sup>3</sup>, Ulrich Hohenester<sup>4</sup>, and Vincenzo Grillo<sup>2\*</sup>*

1. Dipartimento FIM, Università di Modena e Reggio Emilia, via G.Campi 213/a, I-41125,  
Modena, Italy
2. CNR-NANO via G Campi 213/a,I-41125 Modena, Italy
3. Department of Physics, University of Ottawa, 150 Louis Pasteur, Ottawa, Ontario K1N 6N5,  
Canada
4. Institute of Physics, Karl-Franzens-Universität Graz, Universitätsplatz 5, 8010 Graz, Austria

### Experimental set up to measure OAM-resolved EEL spectra.

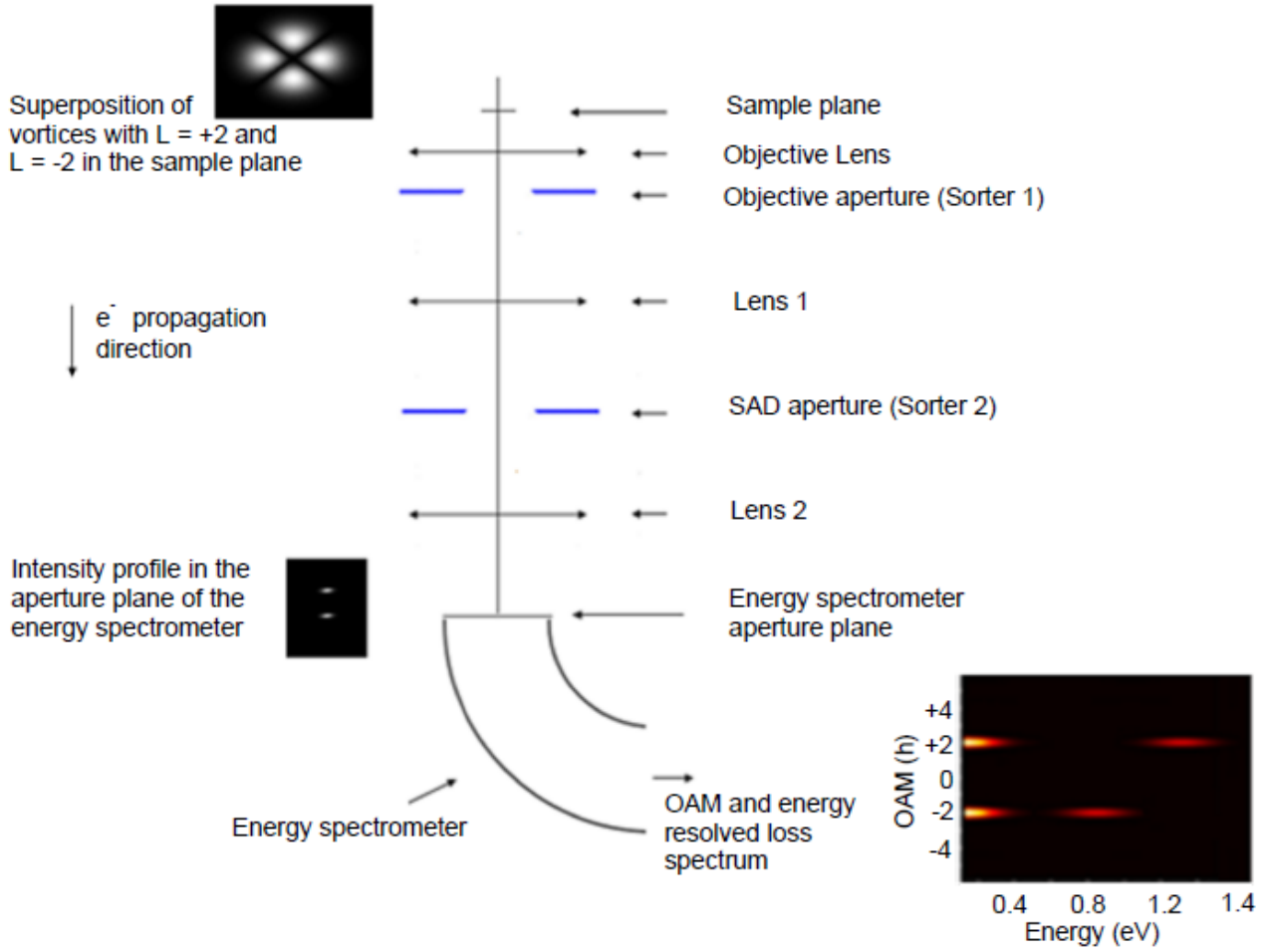


**Figure S1:** Schematic description of the electron optics in the TEM column, necessary to measure OAM resolved EELS spectra

In Figure S1 we present a schematic diagram of the TEM column set up necessary to perform the measurement of an OAM resolved energy loss spectrum.

To do so, we propose to introduce two phase masks in the electron column, after the sample plane, i.e. the Sorter 1 at the level of the Objective aperture and Sorter 2 in correspondence of the SAD aperture plane. It is important to underline that Sorter1 is positioned in the front focal plane of Lens 1, which has in its back focal plane the Sorter 2 element; at the same time, Lens 2 has in its front focal plane the SAD aperture itself and in its back focal plane the aperture of the energy spectrometer.

As outlined in [1] [2] [3][4] the role of Sorter 1 is to perform a log-polar coordinate transformation of the wave function, i.e. to map the azimuthal variation of phase of the electron along a Cartesian coordinate, while the action of Sorter 2 is to introduce the necessary corrections to the defects produced by the first phase element. To clarify this point, we assume an initial beam with orbital angular momentum along  $z$  equal to  $\hbar L$ : the action of the two sorters is to transform the initial

circular phase into a linear phase along the in-plane  $y$  direction, which is transformed by Lens 2 into a spot centered in  $y = \frac{f_2 L}{ak}$ , (where  $k$  is the electron De Broglie wave vector) in the back focal plane of Lens 2. If this plane coincides with the aperture plane of the spectrometer, its role will be to disperse the electrons forming this spot in the perpendicular direction, according to their energies: in this way the OAM resolved EEL spectrum should be obtained through a CCD camera located at the end of the energy spectrometer. Because of the linearity of the overall experimental set up, in the case of a beam with more than one OAM components, in the back focal plane of Lens 2 we expect to observe a series of spots, one for each  $L$  component, whose intensity ratios are equal to the relative weight of the contributes of the different OAM to the electron wave after the sample. In Figure S1 we present how a beam given by the superposition of two vortices, one with  $L = + 2$  and one with  $L = - 2$  is transformed by the overall experimental set up (this has been evaluated using Stem\_cell software [5]).

### Choice of the maximum value $K_{Max}$ to perform the sum in Eq.(6).

To understand if the chosen value for  $K_{Max}$  we have used to perform the sum in Eq.(6) of the main text was correct, i.e. if it was sufficiently large to include the contributions of the different modes to  $\Gamma_\ell(E)$ , we have analysed the behavior of the function  $C_l^m(k_f)$  (namely we singled out the part of  $\Gamma_\ell(E)$  dependent on  $k_f$ ) defined as

$$C_l^m(k_f) = \left| \iint dx dy \psi_{k_f}^\ell(x, y) \phi_m(x, y, q) \psi_i(x, y)^* \right|^2$$

which is such that

$$\Gamma_\ell(E) \propto \sum_k \sum_m^{K_{Max}} \text{Im}(-g_m(E)) C_l^m(k_f)$$

where  $\psi_{k_f}^\ell(x, y)$  is  $J_{|\ell|}(k_f r) e^{i\ell\varphi}$ ,  $\psi_i(x, y)$  is a gaussian beam (taken in the following example with beam waist of 35 nm) and  $\phi_m(x, y, q)$  is the Fourier transform along  $z$  of the potential associated to the plasmon mode  $m$ : according to this definitions,  $K_{Max}$  will be chosen in a way such that for  $k_f > K_{Max}$   $C_l^m(k_f)$  will tend to zero, for each OAM  $l$  and for each mode  $m$ .

As an example, we focus here on the case of the nanodisk: because of the selection rules described in the main text, for a mode  $m$  characterized by azimuthal number  $m_l$  only the functions  $C_{\pm m_l}^m(k_f)$  will be different from zero for some  $k_f$ : so in the following we plot, as examples, the function  $C$  for the dipolar ( $m_l = 1$ ), the quadrupolar ( $m_l = 2$ ) and the hexapolar ( $m_l = 3$ ) modes as a function of  $k_f$  (each function is normalized to its maximum value).

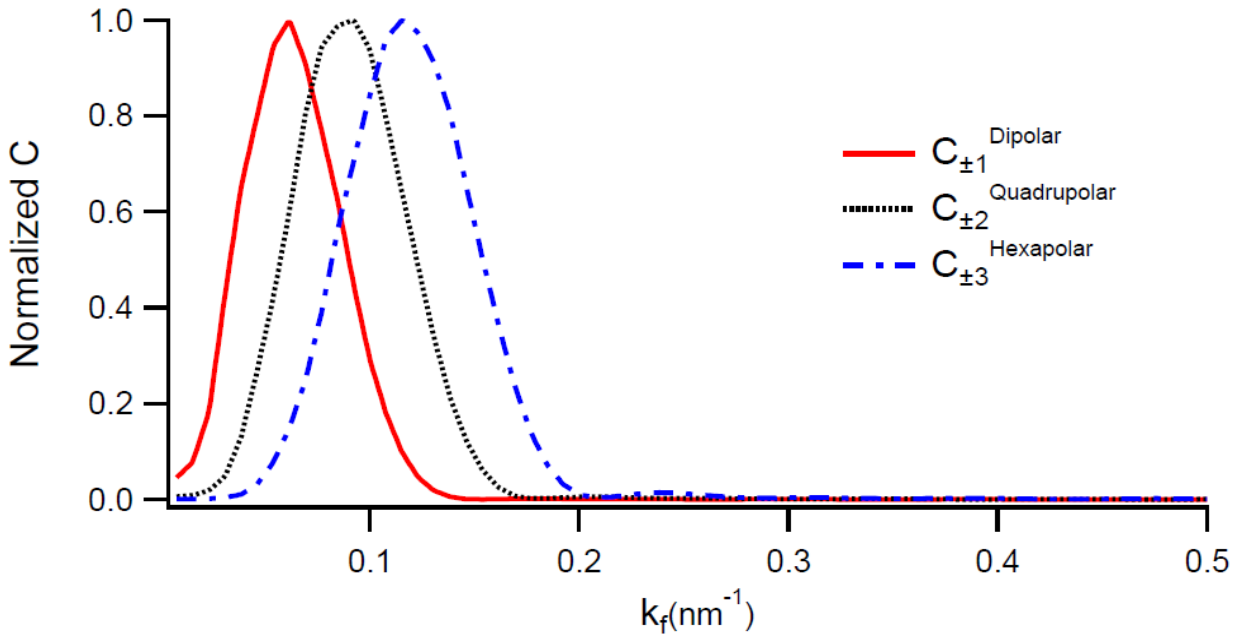


**Figure S2.** Behavior of  $C_{\pm m_l}^m$  for the dipolar, quadrupolar and hexapolar modes of the nanodisk considered in the main text: all the functions have been normalized to their maximum value.

It is immediate to notice, looking at Figure S2, that the choice  $K_{Max} = 0.4nm^{-1}$  is correct because for larger values of  $k_f$  the different functions  $C$  are effectively negligible. This approach has been repeated for the different structures considered in the main text to effectively control the validity of the chosen value of  $K_{Max}$ .

### Convolution procedure

In order to obtain 2D plot which can be compared with the experimental ones, we have performed a convolution procedure: more correctly, we have defined a function

$$\gamma(\ell, E) = \begin{cases} \Gamma_\ell(E) & \text{if } \ell \text{ is an integer number} \\ 0 & \text{if } \ell \text{ is not an integer number} \end{cases}$$

and we have convolved this 2D function with the product of two Gaussian functions, i.e.

$$G(\ell, E) = e^{\frac{-\ell^2}{2\sigma_\ell^2}} e^{\frac{-E^2}{2\sigma_E^2}}$$

where  $\sigma_\ell = \frac{\Delta\ell}{2.355}$  and  $\sigma_E = \frac{\Delta E}{2.355}$ ;

Practically we have computed the convolved spectra as

$$I(\ell, E) = \int dE' \int d\ell' G(\ell', E') \gamma(\ell - \ell', E - E')$$

The quantity  $\Delta\ell$  has been taken equal to  $0.5 \hbar$ , and this takes into account the broadening in the dispersion introduced by the Sorter elements: a decrease in this value could be obtained implementing in the OAM Sorters the Fan-out corrections already applied in the analysis of the OAM of light vortices [6]. At the same time,  $\Delta E$  has been fixed to 0.3 eV, and this broadening accounts for the non monochromaticity of the probing electron beam.

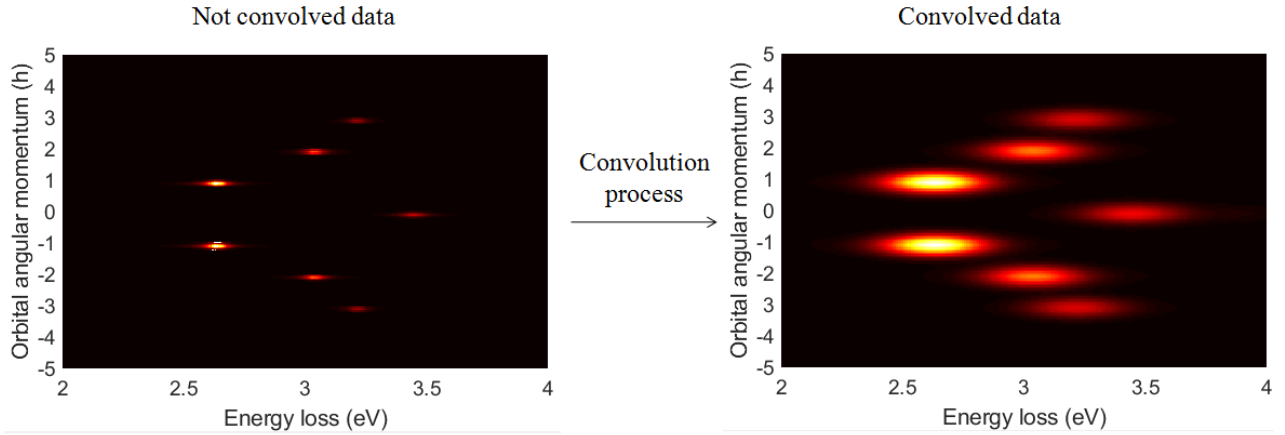


**Figure S3.** On the left, we plot an example of the un-convolved function  $\gamma(\ell, E)$ . On the right the results obtained by the convolution process described before are shown, i.e. the function  $I(\ell, E)$ .

## **OAM decomposition of the potential associated to a plasmon resonance**

In the following we present a possible OAM decomposition of the potential associated to a plasmonic mode: our approach is similar to the one adopted by Juchtmans *et al.*[7].

Let's write the FT along  $z$  of the potential associated to a plasmon resonance  $\alpha$ , computed at  $q = \frac{E_\alpha}{\hbar v}$  as ( $v$  is the incident electron velocity)

$$\phi_\alpha(x, y; q) = \sum_{m=-\infty}^{\infty} \int_0^{\infty} dk c_m(k, q) J_m(kr) e^{im\varphi} \quad S1)$$

i.e. we have developed such potential on the set of functions  $\{J_m(kr)e^{im\varphi}\}$ : the value of the coefficient  $c_m(k, q)$  measures the importance of the term  $J_m(kr)e^{im\varphi}$  for given  $k$  and  $m$  to the overall potential  $V_\alpha$ .

By multiplying 1) on both sides for  $e^{-im_1\varphi}$  and integrating between 0 and  $2\pi$  we find

$$\int_0^{2\pi} d\varphi \phi_\alpha(x, y; q) e^{-im_1\varphi} = 2\pi \int_0^{\infty} dk c_{m_1}(k, q) J_{m_1}(kr) \quad S2)$$

where we have used  $\int_0^{2\pi} e^{i(m-m_1)\varphi} d\varphi = 2\pi\delta_{m,m_1}$ .

By multiplying both sides of 2) for  $J_{m_1}(k'r)r$ , integrating over  $r$  between 0 and  $\infty$  and remembering the property

$$\int_0^{\infty} dr J_{m_1}(k'r) r J_{m_1}(kr) = \delta(k - k')/k$$

we find

$$c_{m_1}(k', q) = \frac{k}{2\pi} \int_0^{\infty} dr r J_{m_1}(k'r) \int_0^{2\pi} d\varphi \phi_\alpha(x, y; q) e^{-im_1\varphi}$$

As we are mainly interested in the contribute of the term defined by the azimuthal number  $m$  to the potential  $\phi$ , we can define a quantity equal to

$$C_{m_1}(q) \equiv \frac{\left| \int_0^{K_{Max}} c_{m_1}(k', q) dk' \right|^2}{\sum_m \left| \int_0^{K_{Max}} c_m(k', q) dk' \right|^2} \quad S3)$$

which is a quantity that gives information about the importance of the term characterized by the azimuthal number  $m_1$  to the overall series in S1).

These coefficients have been obtained from the potential  $\phi_\alpha(x, y; q)$  computed from BEM calculations (see last section), while the integral have been computed numerically approximating the integration over  $r$  with an integral between 0 and a certain  $r_{max}$ , which has been taken much larger than the characteristic dimension of the nanostructure.

In the following we report the OAM decomposition of the potential associated to the plasmonic modes studied in the main text.



### The case of the Nanodisk

As already outlined in the main text, the potentials associated to the plasmonic resonances of a nanodisk are characterized by azimuthal dependencies of the type  $e^{\pm im\varphi}$ : this is effectively confirmed by computing, for different modes, the coefficients defined in S3). As one can easily understand, for a given mode only the functions  $C_{\pm m}$ , for a single  $m$ , will be different from zero.

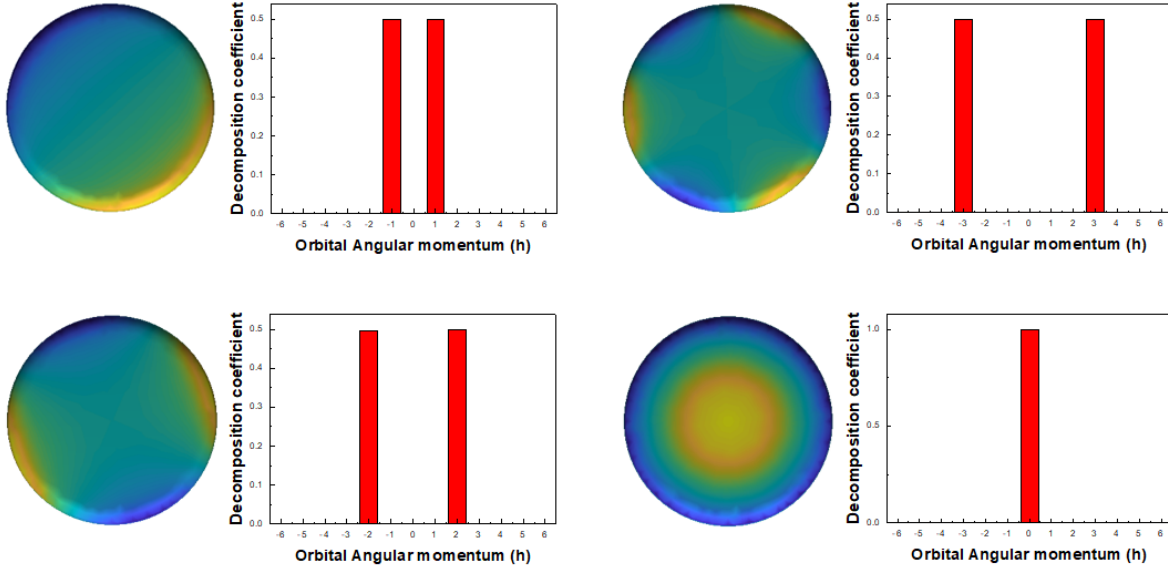


**Figure S4.** Calculation of the coefficients  $C_m$  for the dipolar, the quadrupolar, the hexapolar and the breathing mode of the nanodisk considered in the main text: the surface charge distributions associated to each mode are also displayed. Notice that, as predicted by symmetry, for each resonance, only  $C_{\pm m}$ , for a single  $m$ , is different from zero.

### The case of the nanoellipse

In Figure S5 we show the values of the coefficients  $C_m$  in the case of the nanoellipse considered in the main text, for the two modes which derive from the splitting of the quadrupolar resonance of the nanodisk. Such a nanostructure is obtained from the disk (diameter  $D_{disk} = 70$  nm), by taking the major axis  $a = D_{disk}(1 + \varepsilon_x)$  and the minor one  $b = D_{disk}(1 + \varepsilon_y)$ . We have chosen to fix the area of the ellipse surface equal to the one of the disk, so, imposing this condition we have

$$\varepsilon_y = -\frac{\varepsilon_x}{1 + \varepsilon_x}$$

In the calculations shown in the main text we have taken  $\varepsilon_x = 1/5$ .

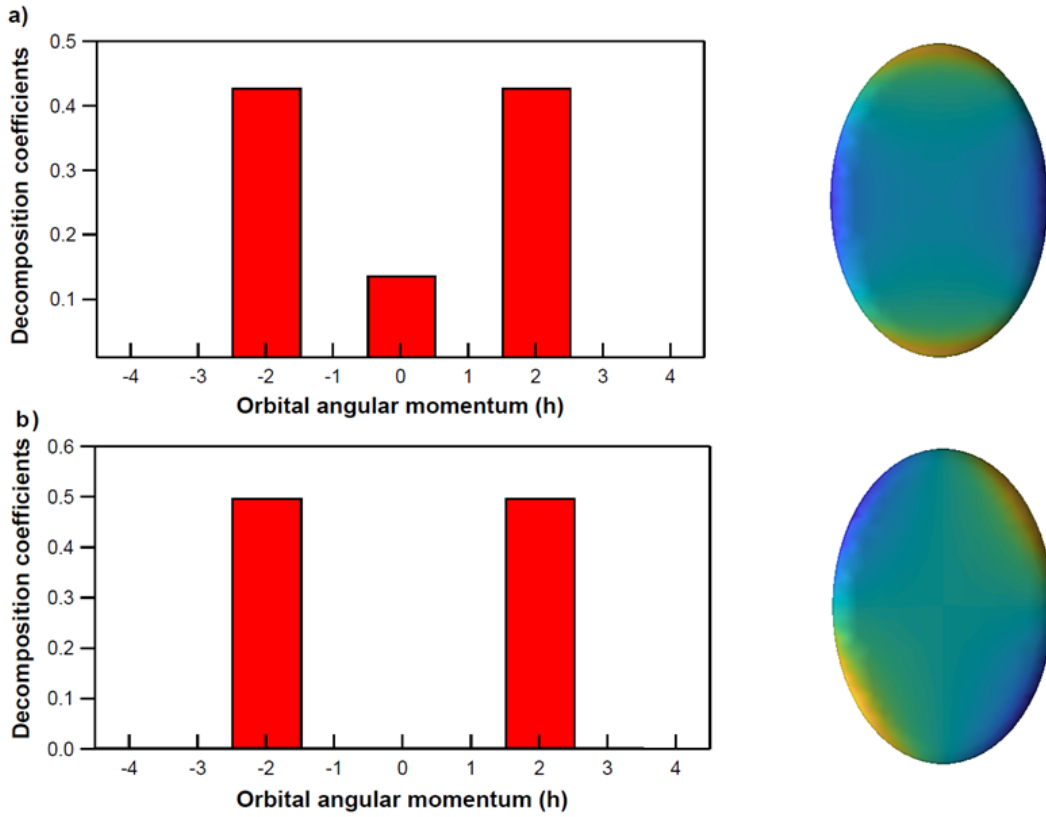


**Figure S5.** Calculation of the coefficient  $C_m$  for the plasmon resonances which derive from the quadrupolar mode of the nanodisk: in a) we show the coefficients for the lower energy mode ( $E = 2.975$  eV), and we notice that only  $C_{\pm 2}$  and  $C_0$  are non negligible, suggesting quadrupolar-breathing modes mixing. In b) we present the same quantities in the case of the resonance at large energy ( $E = 3.05$  eV), in which only  $C_{\pm 2}$  are effectively non zero. The surface charge distributions for both the modes are also shown.

Looking at Figure S5, we can notice that the two modes at energies  $E = 2.975$  eV (Figure S5 a) and  $E = 3.05$  eV (Figure S5 b) have different coefficients  $C_m$ , i.e. the lower energy one have intense contributions from 0 and  $\pm 2$  (suggesting breathing to quadrupolar modes mixing), while the higher energy one has only  $C_{\pm 2}$  different from zero.

To complete the OAM analysis of the plasmon resonances of the nanoellipse we present the decompositions of the modes at energies  $E = 2.4$  eV (Figure S6a),  $E = 2.825$  eV (Figure S6b),  $E =$

3.2 eV (Figure S6c) and  $E = 3.4$  eV (Figure S6d). We notice that for the first two modes only the coefficients  $C_{\pm 1}$  are not negligible (justifying the peaks at these energies observed for  $\Gamma_{\pm 1}$ ), while the mode at energy  $E = 3.2$  eV has only  $C_{\pm 3}$  strongly different from zero, while for the excitation at energy  $E = 3.4$  eV only  $C_0$  is effectively non zero: in this way the peaks for  $\Gamma_{\pm 3}$  and  $\Gamma_0$  at the energies of these modes are understood.

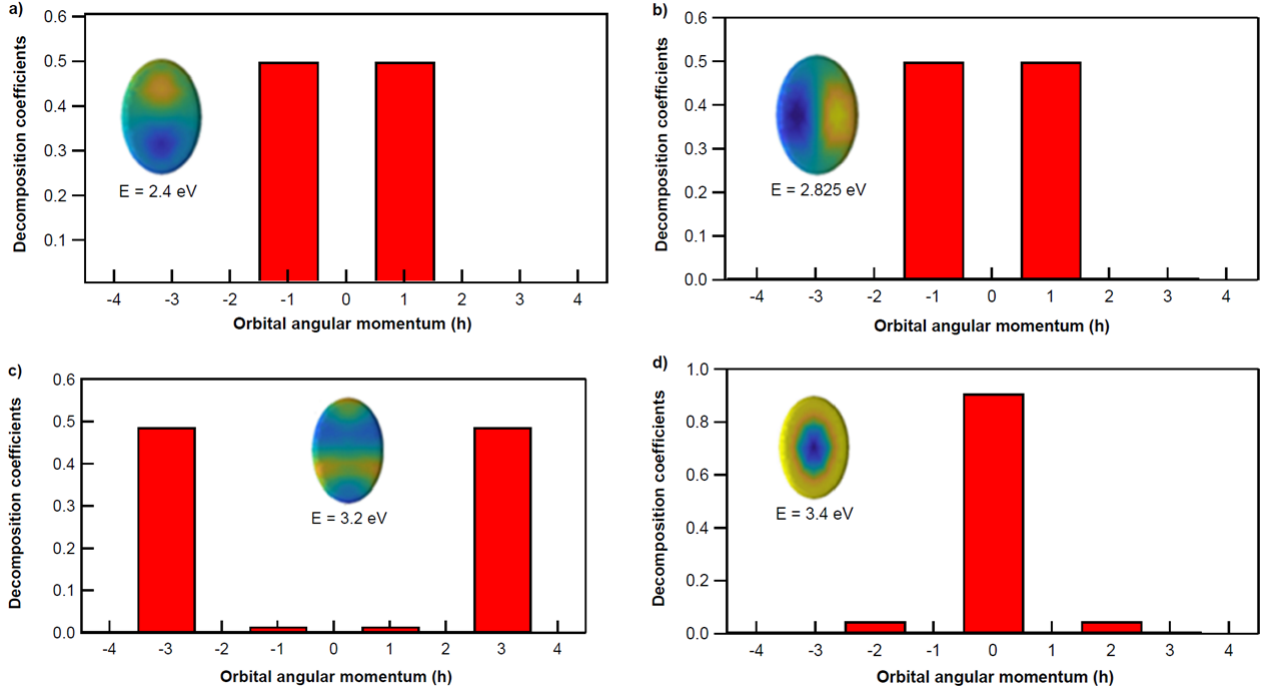


**Figure S6.** Calculation of the coefficients  $C_m$  for the modes of the nanoellipse a) with energy  $E = 2.4$  eV, b) with energy  $E = 2.825$  eV, c) with energy  $E = 3.2$  eV and d) with energy  $E = 3.4$  eV. Notice that the modes in a) and b) have only  $C_{\pm 1}$  different from zero, justifying the peaks for  $\Gamma_{\pm 1}$  at the energies of these resonances. The excitation considered in c) has only  $C_{\pm 3}$  non zero, while the one in d) is characterized by a large  $C_0$ , and so we respectively observe peaks for  $\Gamma_{\pm 3}$  and  $\Gamma_0$  at the energy of these modes. The insets show the surface charge distributions characteristic of each mode.

### The case of the plasmonic metamolecule

We present here the decomposition of the first three lower energy modes of the precedently described plasmonic metamolecule. To further clarify the comprehension of the decomposition defined by Eq. S1, we also plot for each mode the in plane spatial behavior of  $\phi(x, y; q)$  computed at  $q = \frac{E_\alpha}{\hbar v}$ .

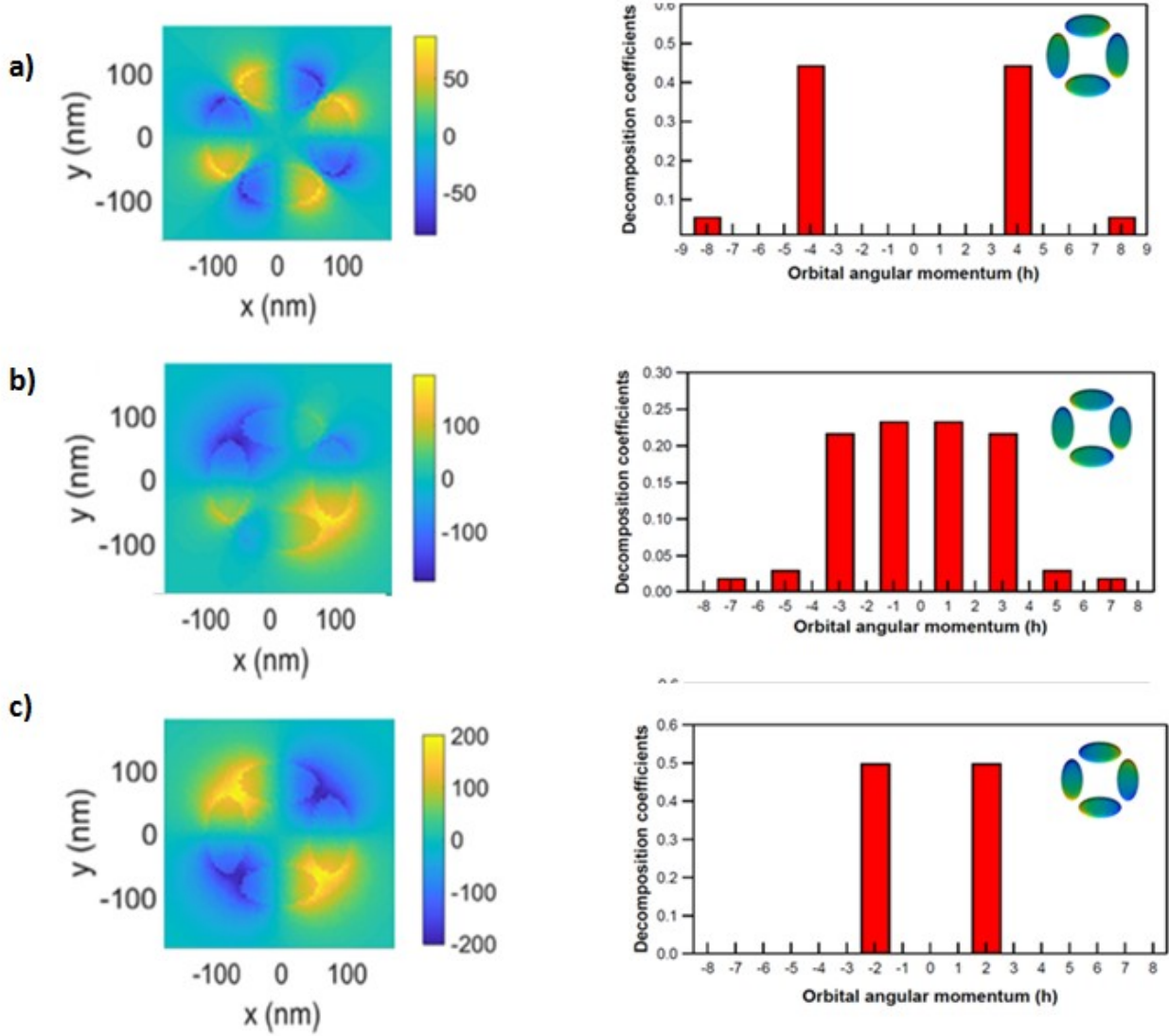


**Figure S7.** Calculation of the coefficients  $C_m$  for the modes of the plasmonic metamolecule considered in the main text: in the left column we also present the profiles of  $\phi_\alpha(x, y; q)$  for these three resonances evaluated with BEM theory.

From Figure S7a, we can notice that the leading components of the potential associated to the first mode are those for  $\pm 4$ , as predicted in the main text: we point out that this is also clear from the fact that the potential changes eight times its sign in a complete circular path around the center of the plasmonic metamolecule, which is the characteristic behavior of a function with an azimuthal

profile determined by  $e^{\pm 4i\varphi}$ : the same reasoning can also be applied to the higher energy mode among these, in which the most important contribute comes from  $\pm 2$  (see Figure S7c).

Finally the presence of peaks for  $\Gamma_{\pm 1}$  and  $\Gamma_{\pm 3}$  at the energy of the second considered resonance is now fully understood looking at Figure S7b, as for this mode the strongest decomposition coefficients are  $C_{\pm 1}$  and  $C_{\pm 3}$ .

### The case of the chiral structure

We now present the calculated coefficients  $C_m$  for the resonance found at  $E = 1.53$  eV and  $E = 2.03$  eV of the chiral structure introduced in the main text (we point out that this structure possesses also plasmonic excitations at energies lower than 1 eV, but we do not consider them here, as in real life experiment it could be very difficult to separate their contributes to the electron losses from the tail of the zero loss peak).

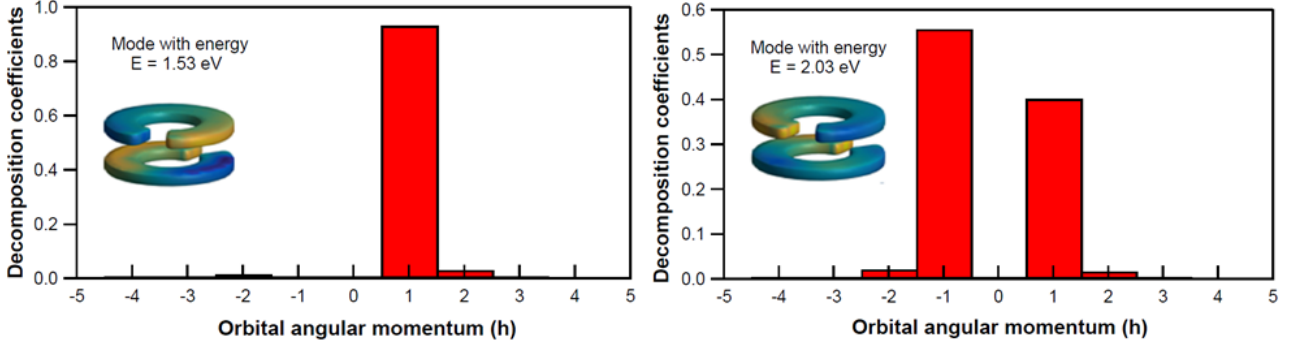


**Figure S8.** Coefficients  $C_m$  for the modes at  $E = 1.53$  eV and  $E = 2.03$  eV for the chiral structure: notice that for the lower energy one only the coefficient  $C_{+1}$  turns out to be effectively not negligible.

It is simple to realize (looking at Figure S8) that the mode at  $E = 1.53$  eV (from now on called mode  $a$ ) has only  $C_1$  different from zero, so this suggests that the potential  $\phi_a(x, y; q) \approx f_a(r)e^{i\varphi}$ , and that's why in the OAM resolved EEL spectra only a peak for  $\Gamma_{-1}$  is observed; at the same time the mode at energy  $E = 2.03$  eV has a stronger contribution from -1 than from +1, and so we can explain why at this energy  $\Gamma_{+1}$  turns out to be more intense than  $\Gamma_{-1}$ .

The fact that  $\phi_a(x, y; q) \approx f_a(r)e^{i\varphi}$  can also be understood looking at the phase profile of the function  $\phi_a(x, y; q)$  (which is complex once the mirror symmetry is lost): this is reported in Figure S9: notice that it is characterized by an on axis singularity, with topological charge equal to +1, i.e. the characteristic phase of a function  $\phi_a(x, y; q) \approx f_a(r)e^{i\varphi}$  (see for example the review [8])

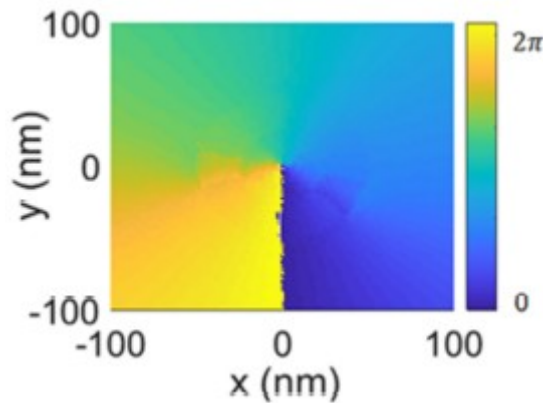


**Figure S9.** In plane phase profile of the potential associated to the mode with excitation energy  $E = 1.53$  eV.

### **Methods to compute the OAM resolved loss function through Eq.6**

The functions implemented in the MNPBEM toolbox has been exploited to discretize the surface of the considered plasmonic nanoparticles; we have then computed the surface charge distributions associated to the different plasmonic resonances of the nanostructure as

$$\int d\mathbf{s}' F(\mathbf{s}, \mathbf{s}') \sigma_m(\mathbf{s}') \xrightarrow{\text{surface discretization}} \sum_j \Delta \mathbf{s}_j F(\mathbf{s}_i, \mathbf{s}_j) \sigma_m(\mathbf{s}_j) = 2\pi \lambda_m \sigma_m(\mathbf{s}_i) \quad S4$$

where  $\mathbf{s}_i$  is the position of the center of the  $i^{\text{th}}$  element in which the nanostructure surface has been discretized, while  $\sigma_m(\mathbf{s}_j)$  indicates the surface charge distribution associated to mode  $m$ , and

$$F(\mathbf{s}, \mathbf{s}') = \frac{-\mathbf{n}_s \cdot (\mathbf{s} - \mathbf{s}')}{|\mathbf{s} - \mathbf{s}'|^3}$$

being  $\mathbf{n}_s$  the normal vector to the surface of the nanostructure at  $\mathbf{s}$ : the sum appearing in Eq. S4 is performed on the nanostructure discretized surface elements. From this equation, it is simple to notice that computing the surface charge modes means solving a linear eigenvalue problem, which directly provides the eigencharges: notice that the corresponding eigenvalues determines the position in energy of the peaks for the spectral functions defined in the main text. The quantities  $\sigma_m(\mathbf{s}_j)$  and  $\lambda_m$  are computed through the MNPBEM toolbox.

The potential associated to the resonance  $m$ ,  $\phi_m$ , can be written as

$$\phi_m(x, y, z) = \int \frac{\sigma_m(\mathbf{s}')}{|\mathbf{r} - \mathbf{s}'|} d\mathbf{s}'$$

where the integral is again performed as a sum over the nanostructure surface elements. From this expression it is easy to compute the Fourier transform along  $z$ , i.e.

$$\phi_m(x, y, q) = \int_{-\infty}^{+\infty} dz e^{-iqz} \phi_m(x, y, z) = \int d\mathbf{s}' \sigma_m(\mathbf{s}') \int_{-\infty}^{+\infty} dz \frac{e^{-iqz}}{|\mathbf{r} - \mathbf{s}'|}$$

which has been solved through the tabulated integral

$$\int_{-\infty}^{+\infty} dz \frac{e^{ibz}}{\sqrt{a^2 + z^2}} = 2K_0(ab)$$

where  $K_0$  is a modified Bessel function of second kind of order zero. In this way the function  $\phi_m(x, y, q)$  appearing in Eq.6 in the main text is known, and the OAM resolved loss functions can be evaluated as a sum over the different plasmonic resonances.

## References

- 
- (1) Grillo, V.; Tavabi, A.H.; Venturi, F.; Larocque H.; Balboni, R.; Gazzadi, G.C.; Frabboni, S.; Lu, P.H.; Mafakheri, E.; Bouchard, F.; Dunin-Borkowski R.E.; Boyd, R.W.; Lavery M.P.J.; Padgett, M.J.; Karimi, E., Measuring the orbital angular momentum spectrum of an electron beam. *Nat. Commun.* **2017**, 8, 15536.
  - (2) Berkhout, G.C.G.; Lavery, M.P.J.; Courtial, J.; Beijersbergen, M.W.; Padgett, M.J., Efficient Sorting of Orbital Angular Momentum States of Light *Phys. Rev. Lett.* **2010**, 105, 153601.
  - (3) Hossack, W.; Darling, A.; Dahdouh, A., Coordinate Transformations with Multiple Computer-generated Optical Elements *J. Mod. Opt.* **1987**, 34, 1235–1250.
  - (4) McMorran, B.J.; Harvey, T.R.; Lavery, M.P., Efficient sorting of free electron orbital angular momentum. *New J. Phys.*, **2017**, 19, 023053
  - (5) Grillo, V.; Rotunno, E., STEM\_CELL: A software tool for electron microscopy: Part I—simulations *Ultramicroscopy* **2013**, 125, 97-111.
  - (6) Mirhosseini, M.; Malik, M.; Shi, Z.; Boyd, R.W., Efficient separation of the orbital angular momentum eigenstates of light. *Nat. Commun.* **2013**, 4, 2781.
  - (7) Juchtmans, R.; Verbeeck, J., Orbital angular momentum in electron diffraction and its use to determine chiral crystal symmetries. *Phys. Rev. B*, **2015**, 92, 134108.
  - (8) Bliokh, K.Y.; Ivanov, I.P.; Guzzinati, G.; Clark, L.; Van Boxem, R.; Béch , A.; Juchtmans, R.; Alonso, M.A.; Schattschneider, P.; Nori, F.; Verbeeck, J., Theory and applications of free-electron vortex states *Physics Rep.* **2017**, 690, 1-70.